

Sn[B₂O₃F₂]*—*The First Tin Fluorooxoborate as Possible NLO Material

Stephan G. Jantz, Marwin Dialer, Lkhamsuren Bayarjargal, Björn Winkler, Leo van Wüllen, Florian Pielhofer, Jakoah Brgoch, Richard Wehrich, and Henning A. Höppe*

Herein, the crystal structure as well as second-harmonic-generation (SHG), thermal and spectroscopic properties of Sn[B₂O₃F₂] (TFB = tin-fluorooxoborate) are presented. TFB adopts a novel non-centrosymmetric crystal structure, which is determined by single-crystal X-ray diffraction (XRD) (*P*31*m*, *Z* = 1, *a* = 4.5072(2) Å, *c* = 4.7624(3) Å) and comprises [B₂O₃F₂]²⁻ layers consisting solely of BO₃F tetrahedra; the covalent B–F bonds are unequivocally localized via solid-state NMR spectroscopy as well as density functional theory (DFT) calculations. TFB is insensitive to air and moisture, shows a stronger SHG intensity than K[H₂PO₄] (KDP) and a bandgap of ≈5 eV. The thermal decomposition yields two new borate fluorides.

1. Introduction

Nonlinear optical (NLO) materials are of high relevance due to their application using the second-harmonic-generation (SHG) effect resulting in frequency doubling of laser wavelengths since the first experimental observation by Franken et al.^[1] One of the most prominent examples are green laser pointers, in which for human eyes highly perceptible green light is generated by frequency doubling of an infrared laser beam. Recently, SHG materials with large bandgaps attracted high interest due to their higher efficiency and materials' stability.^[2,3] As a non-centrosymmetric crystal structure is a compulsory prerequisite for NLO effects, borates with their most common, non-centrosymmetric building blocks BO₃ (point group *D*_{3h}) and BO₄ (*T*_d) are a very good choice and already yielded prominent examples like β-Ba[B₂O₄] (BBO) and LiB₃O₅ (LBO) competing well with K[H₂PO₄] (KDP).^[4–6]

There are different strategies to facilitate the formation of non-centrosymmetric structures. A really interesting one is the exfoliation of 2D materials such as WSe^[7] and MoS₂^[8,9] useful for new applications in optoelectronics devices allowing for an

electrical control of the respective materials' SHG properties. Highly interesting as efficient large bandgap SHG materials are borates like KBBF, i.e., KBe₂BO₃F₂, providing a layered structure.^[10] According to these the coplanar configuration of the non-centrosymmetric building units promotes birefringence and SHG. Moreover, the weak ionic interactions mediated via K⁺-F⁻ contacts between adjacent [Be₂BO₃F₂] layers strengthen its layer habit further. Recently, with Cs₃Zn₆B₉O₂₁ (CZB)^[11] within the same family of compounds another highly promising borate was presented, both of special interest

because of their large bandgap allowing SHG also in the UV regime. A close relative to KBBF is Sr₂Be₂B₂O₇ (SBBO),^[12] comprising [Be₂(BO₃)₂O] layers. Both materials contain beryllium which is not favored in applications due to the high toxicity of Be²⁺ ions.

Fluorooxoborates should comprise sufficiently large bandgaps in the UV as well as preferential formation of non-centrosymmetric structures, thus making them ideal candidates for SHG materials in the UV. Beyond that, they normally combine the birefringence promoting triangular BO₃ or tetrahedral BO₃F moieties providing terminal fluorine atoms with a proclivity for weak coordination.^[13–26] Recent calculations^[27] as well as our own results^[28] confirm these considerations and suggest a boost for NLO materials based on so-called fluorooxoborates.

Apparently, nature normally strives for high symmetry, and therefore—from a solid state chemists point of view—non-centrosymmetric structures are facilitated by the presence of suited basic building blocks like the mentioned triangular or tetrahedral ones. But frequently, also these are arranged centrosymmetrically in a crystal structure. Our approach therefore uses as second driving force the choice of such basic building

S. G. Jantz, M. Dialer, Prof. H. A. Höppe
Lehrstuhl für Festkörperchemie
Universität Augsburg
Universitätsstraße 1, Augsburg D-86159, Germany
E-mail: henning@ak-hoepppe.de
Dr. L. Bayarjargal, Prof. B. Winkler
Institut für Geowissenschaften
Universität Frankfurt
Altenhöferallee 1, Frankfurt D-60438, Germany

Prof. L. van Wüllen
Lehrstuhl für Chemische Physik und Materialwissenschaften
Universität Augsburg
Universitätsstraße 1, Augsburg D-86159, Germany
Dr. F. Pielhofer, R. Wehrich
Lehrstuhl für Ressourcenstrategie
Universität Augsburg
Universitätsstraße 1, Augsburg D-86159, Germany
Prof. J. Brgoch
Department of Chemistry
University of Houston
Houston, TX 77204, USA

 The ORCID identification number(s) for the author(s) of this article can be found under <https://doi.org/10.1002/adom.201800497>.

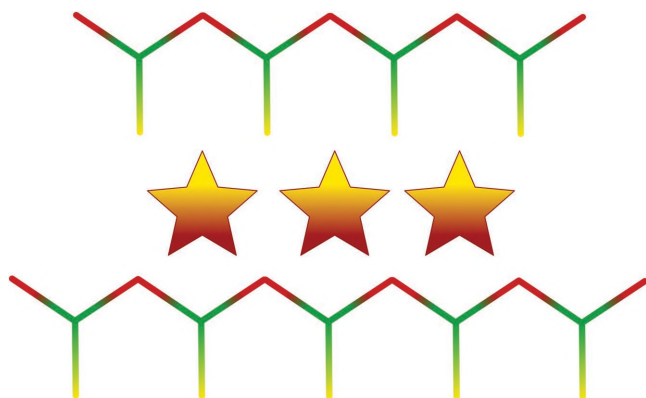


Figure 1. Simplified structure scheme showing the interaction of a bidentate cation (star with sterically active lone-pair in yellow, coordinating end in red) with a stronger coordinating oxygen (red) and a weaker coordinating fluorine (yellow) end of a layered anion.

blocks acting as bidentate ligands—e.g., $\text{O}-\text{BO}_2-\text{F}$ tetrahedra—with differing coordination behavior in combination with bidentate cations like s^2 ions like Sn^{2+} or Bi^{3+} in which the sterically active lone-pair plays the role of the weakly coordinating end—regardless of the actual orbital character these prefer a highly nonisotropic coordination behavior with small coordination numbers. In such fluorooxoborates the weaker end should interact with the weaker coordinating fluorine atoms whilst the stronger end interacts with oxygen atoms. Thus non-centrosymmetric structures should be favored, especially in case of a layered anion as schematically shown in **Figure 1**.

Therefore the tendency towards non-centrosymmetric crystal structures should be enhanced by replacing one or two oxygen ligands by fluorine atoms in fluorooxoborates. Because the first fluorooxoborates were investigated mainly with focus on their ionic conductivity, they comprised alkali metal ions as cations,^[14–17,19,25,29] and only in rare cases other cations like trivalent bismuth.^[13,30] Nevertheless their nonlinear optical properties were investigated, too. The lithium and bismuth^[13,15–17] fluorooxoborates $\text{LiB}_6\text{O}_9\text{F}_2$, $\text{Li}_2\text{B}_6\text{O}_9\text{F}_2$, $\text{Li}_2\text{B}_6\text{O}_9\text{F}_2$, $\text{BiB}_2\text{O}_4\text{F}$ as well as the recently published series $\text{MB}_4\text{O}_6\text{F}$ ($\text{M} = \text{NH}_4, \text{Na}, \text{K}, \text{Rb}, \text{Cs}$) show a SHG effect, the latter already with deep UV bandgaps.^[22,31–33] For $\text{LiB}_6\text{O}_9\text{F}_2$ a more in-depth density functional theory (DFT)-based ab initio investigation on this topic was performed and revealed that the coefficients of the second order nonlinear susceptibility were comparable to those of KDP.^[20] Very recently, the first fluorooxoborates of calcium and strontium, i.e., $\text{M}_2\text{B}_{10}\text{O}_{14}\text{F}_6$ ($\text{M} = \text{Ca}, \text{Sr}$), were described; they show a highly interesting structural relationship with the aforementioned $\text{Sr}_2\text{Be}_2\text{B}_2\text{O}_7$ ^[12] and are obtained by formally replacing the tetrahedral BeO_4 moieties with BO_3F .^[34,35]

In the course of our systematic investigations of silicate-analogous materials^[36–39] we also focus on inorganic fluoroderivatives of oxo-anions like phosphates, borates and tungstates.^[26] Recently, we discovered the very first alkaline-earth fluorooxoborate $\text{Ba}[\text{B}_4\text{O}_6\text{F}_2]$ which crystallizes centrosymmetrically—in contrast to a prediction^[27]—and could be doped with Eu^{2+} to show efficient ultraviolet luminescence proving the weak coordinative force expected in such materials;^[28] here a simple spherical cation lead to a centrosymmetric structure. In

this context we now examined the system $\text{SnF}_2-\text{B}_2\text{O}_3$ providing the bidentate cation Sn^{2+} and obtained a novel fluorooxoborate, $\text{Sn}[\text{B}_2\text{O}_3\text{F}_2]$ (tin-fluorooxo-borate, TFB), showing a remarkable structure and highly promising NLO properties. Further investigations of this compound lead to two decomposition products which turned out to be borate fluorides.

2. Results

Based on our new approach (Figure 1) we synthesized the very first tin fluorooxoborate, $\text{Sn}[\text{B}_2\text{O}_3\text{F}_2]$ (TFB), starting from SnF_2 and B_2O_3 in an equimolar ratio in evacuated silica ampoules at 350 °C. It was obtained as phase-pure (Figure S1 in the Supporting Information), coarsely crystalline and colorless powder.

2.1. Crystal Structure of $\text{Sn}[\text{B}_2\text{O}_3\text{F}_2]$

TFB crystallizes in a new structure type in the trigonal, non-centrosymmetric space group $P31m$ (no. 157) with one formula unit per unit cell. The crystal structure is built up by corner-sharing BO_3F tetrahedra, forming a 2D infinite layer perpendicular to the c axis (**Figure 2a**). The B–F bonds are aligned perpendicular to this layer pointing exclusively along the same direction. The layers comprise a honeycomb structure consisting of Sechser (twelve-membered) rings of BO_3F tetrahedra (**Figure 2b**). The Sn^{2+} cations are located in the center of each honeycomb, shifted along $[001]$, forming own layers. The anisotropic displacement parameters reveal no anomalies.

The structural motif of layers consisting of condensed tetrahedra with the terminal atoms pointing towards a unitary direction is found similarly as part of the structures of, e.g., BiB_3O_6 ,^[40] the mineral lizardith $\text{Mg}_3(\text{Si}_2\text{O}_5)(\text{OH})_4$,^[41] or $h\text{-ScAlOC}$.^[42,43] However, $\text{Sn}[\text{B}_2\text{O}_3\text{F}_2]$ is the very first fluorooxoborate comprising this arrangement in this variant as unique structural motif.

The crystal structure can also be understood as a primitive packing of hexagonal tin layers with the boron atoms situated in all trigonal prismatic voids. While the fluorine atoms occupy half of the resulting tetrahedral voids formed by a boron and three tin atoms, the oxygen atoms are found in tetrahedral voids formed by two boron and two tin atoms—shifted from their center toward the trigonal plane of two neighboring boron atoms and a tin atom.

The observed B–O and B–F distances of 1.4740(11) and 1.413(4) Å, respectively, match very well with the sum of the effective ionic radii^[44] of 1.49 and 1.42 Å, respectively. The angles O–B–O (109.12(11)°) and O–B–F (109.82(11)°) are also close to the tetrahedral angle. Thus the deviation of the BO_3F moieties in $\text{Sn}[\text{B}_2\text{O}_3\text{F}_2]$ from a tetrahedron is only 0.08%; it was calculated applying the method suggested by Balić-Zunić and Makovicky based on all ligands enclosing spheres on experimental data.^[45,46] A concise description of the method has been given earlier.^[39]

The Sn^{2+} cations are coordinated threefold by oxygen atoms, occupying the top of a trigonal pyramid. The Sn–O distance amounts to 2.2695(14) Å and matches well with the sum of the ionic radii of 2.31 Å.^[44,47] Interestingly, the O–Sn–O angles

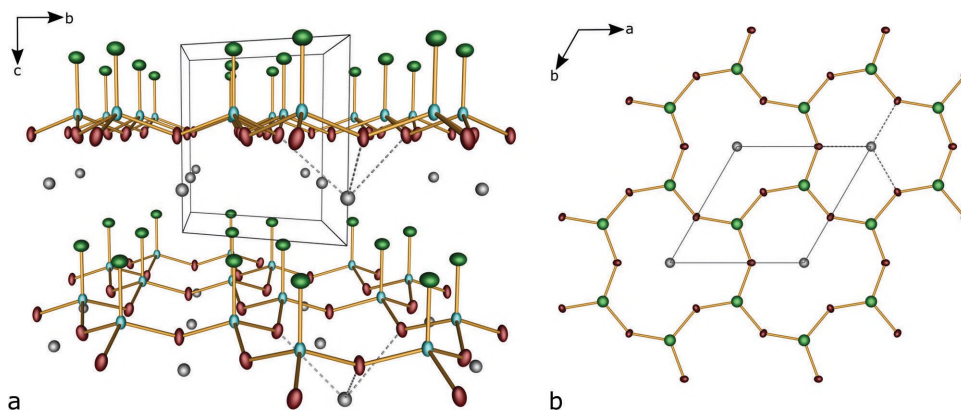


Figure 2. The crystal structure of $\text{Sn}[\text{B}_2\text{O}_3\text{F}_2]$. a) Perspective view along $[100]$, visualizing the layered structure of $\text{Sn}[\text{B}_2\text{O}_3\text{F}_2]$ and the coordination of the Sn^{2+} cations. b) Parallel view along $[001]$, illustrating the “honeycomb” structure; the boron atoms are covered by the fluorine atoms. Tin gray, boron turquoise, oxygen dark red, fluorine green; all atoms are drawn with their displacement ellipsoids at a 75% probability level; the unit cell is drawn as solid black line; dashed grey lines depict Sn–O coordination bond.

amount to $85.22(5)^\circ$ and are therefore close to those found in $\text{Sn}(\text{OH})_2^{2+}$ ions in accordance with an s-character lone pair and p-type bonding orbitals to the coordinating oxygen atoms suggesting right angles. With a distance of $\approx 2.97 \text{ \AA}$, the fluorine atoms of the layer below are too distant to contribute significantly to the coordination environment, which was confirmed by electrostatic calculations based on the MAPLE concept (Madelung part of Lattice Energy).^[48–50] The charges obtained from these calculations are listed in Table S2 in the Supporting Information. Moreover, we confirmed these charges by BORN charges obtained from the theoretical calculation of the optical properties, shown in Table S3 (Supporting Information). Thus our structural model of $\text{Sn}[\text{B}_2\text{O}_3\text{F}_2]$ (MAPLE = $24\,281 \text{ kJ mol}^{-1}$) is electrostatically consistent ($\Delta = 0.27\%$) compared to the sum (MAPLE = $24\,345 \text{ kJ mol}^{-1}$) of the binary compounds SnF_2 (ICSD no. 308;^[51] MAPLE = $27\,59 \text{ kJ mol}^{-1}$) and B_2O_3 (ICSD no. 36066;^[52] MAPLE = $21\,586 \text{ kJ mol}^{-1}$).

2.2. Nonlinear Optical Properties

According to the lack of an inversion center in space group $P31m$ (no. 157) adopted by the crystal structure of $\text{Sn}[\text{B}_2\text{O}_3\text{F}_2]$, the title compound should show nonlinear optical properties. Therefore, we investigated the SHG response of $\text{Sn}[\text{B}_2\text{O}_3\text{F}_2]$ to prove the absence of an inversion center and, moreover, to elucidate its efficiency with regard to well known second-harmonic generation materials, such as $\text{K}[\text{H}_2\text{PO}_4]$ (KDP), quartz, or BaTiO_3 .

Table 1 shows the intensity of the SHG signal of $\text{Sn}[\text{B}_2\text{O}_3\text{F}_2]$ in comparison to several reference compounds. The SHG intensity for $\text{Sn}[\text{B}_2\text{O}_3\text{F}_2]$ is much higher than that of quartz. The strong SHG signal unambiguously implies that $\text{Sn}[\text{B}_2\text{O}_3\text{F}_2]$ crystallizes in a non-centrosymmetric space group. The space group $P31m$ has five independent SHG coefficients, which contribute to the effective SHG coefficient of the powder sample.^[53] The ratio of the sample signal to a quartz signal is ≈ 19 . This ratio is close to the corresponding ratios of the nonphase matchable BaTiO_3 or phase matchable KDP reference samples. Therefore, we cannot distinguish between the case where the

effective SHG coefficient of the sample is small, like in KDP, and the sample is phase matchable, or where the sample is nonphase matchable and has a high effective SHG coefficient, like BaTiO_3 . The correlation between the grain size and the intensity of the SHG signal would potentially allow to discriminate between phase matchable and nonphase matchable materials^[54] but such measurements were beyond the scope of the present study.

2.3. $\text{Sn}[\text{B}_2\text{O}_3\text{F}_2]$ Viewed from Theory

Furthermore, DFT calculations were performed on the vibrational spectra and the electronic structure of $\text{Sn}[\text{B}_2\text{O}_3\text{F}_2]$. Structural optimizations with different xc-functionals and optionally included dispersion correction and the Fock-exchange containing hybrid HSE06 show excellent agreement with the experimental lattice parameters. Based on the optimized structure, the IR and Raman spectra were calculated and simulated in order to interpret the experiment (see below).

The bonding situation is revealed by the electronic band structure (see Figure 3). $\text{Sn}[\text{B}_2\text{O}_3\text{F}_2]$ is a large gap semiconductor with an indirect bandgap, with the valence band maximum located at K and the conduction band minimum at M. The values for the bandgap obtained with different codes and functionals are 4.97 eV (FPLO PBE) and 5.19 eV (CRYSTAL HSE06)—these values fit very well with our experimentally determined one of 5.1(1) eV. A larger discrepancy between the highest and the second highest band is found with HSE06,

Table 1. Observed SHG intensities on powder samples relatively against quartz.

Sample	SHG intensity/counts	$I_{\text{SHG}}/I_{\text{quartz}}$
Quartz	769(290)	1
Al_2O_3	4(10)	0
KDP ($\text{K}[\text{H}_2\text{PO}_4]$)	13007(1840)	16.9
BaTiO_3	15186(970)	19.7
$\text{Sn}[\text{B}_2\text{O}_3\text{F}_2]$	14370(1664)	18.7

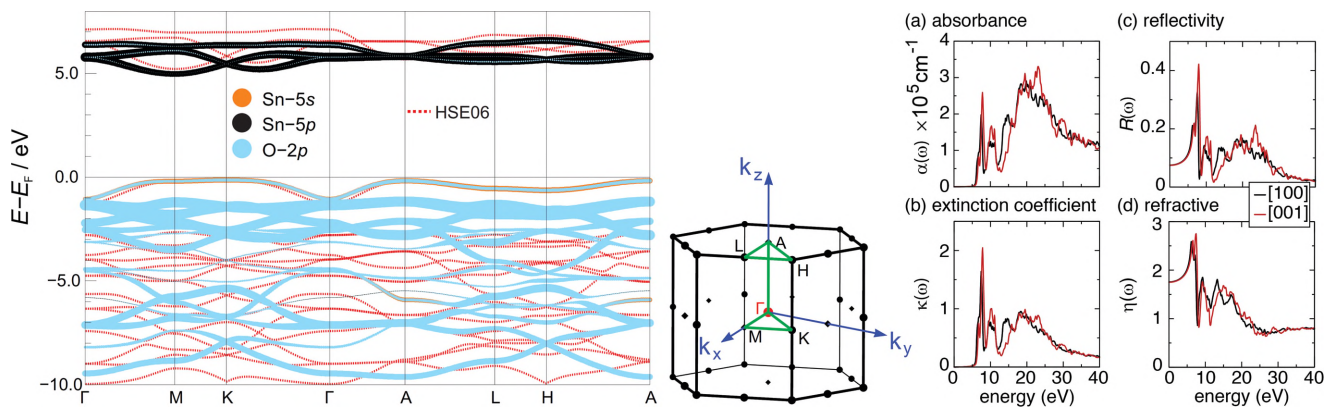


Figure 3. (Left) Electronic band structure and Brillouin zone of $\text{Sn}[\text{B}_2\text{O}_3\text{F}_2]$; GGA versus HSE06 (red dotted lines) results; weighted orbital contributions are plotted onto the PBE bands as dots. (Right) a) Absorbance, b) extinction coefficient, c) reflectivity, and d) refractive spectrum calculated based on the frequency-dependent complex dielectric function using HSE06.

otherwise no big difference is observed for the band alignment with the two functionals. The valence band is mainly composed of Sn-5s and O-2p orbitals, whereas the conduction band consists of almost exclusively Sn-5p contributions. To illustrate the activity of the lone-pair of Sn^{2+} we also carried out a direct space analysis of the charge density was carried out by calculating the electron localization function (ELF) which is shown in Figure S2 in the Supporting Information.

The linear optical properties can be obtained from the frequency-dependent complex dielectric response. Based on these calculations, the frequency dependent optical properties show that from the valence band minimum (≈ 5 eV) to 10 eV above the conduction band maximum, the optical response is nearly isotropic, which is in agreement with the similar lattice parameters of the hexagonal crystal structure. However, unexpectedly there is noticeable anisotropic behavior from 10 to 15 eV and the high-energy region is again isotropic. Specifically, analyzing the calculated optical response shows the absorption coefficient $\alpha(\omega)$, plotted in Figure 3a, has an onset at ≈ 5 eV stemming from the electronic transition between the Sn-5s and oxygen 2p states that compose the valence band and the Sn-5p orbitals that set the conduction band. This absorption edge indicates that $\text{Sn}[\text{B}_2\text{O}_3\text{F}_2]$ is indeed transparent to the visible region as experimentally observed. The extinction coefficient (Figure 3b) suggests this calculated absorption is also moderately intense with a maximum of 1.64 at 7.4 eV above the conduction band maximum. The absorption is further supported by the calculated reflectivity, $R(\omega)$, that shows less than 10% of the incident energy is absorbed up to 4.4 eV (Figure 3c). These results ensure that this compound is not absorbing a significant fraction of visible or ultraviolet light. Finally, further analysis of the optical properties shows the refractive index, plotted in Figure 3d, has a static value of 1.75 at $\eta(0)$ and reaches a maximum of 2.58 at 6.2 eV before reaching a constant, minimum of ≈ 0.8 above 25 eV.

2.4. Spectroscopic Properties

2.4.1. Solid State NMR Spectroscopy

Solid state NMR spectroscopy was applied to corroborate the findings from the crystal structure analysis including

a direct verification of the presence of BO_3F moieties. The ^{11}B -, ^{19}F -, and ^{119}Sn -MAS NMR spectra of $\text{Sn}[\text{B}_2\text{O}_3\text{F}_2]$ are shown in Figure 4. In the ^{11}B -MAS NMR spectrum, only a single narrow line at 0 ppm, accompanied by a set of spinning sidebands may be identified. From a simulation of the spectrum employing the DMFIT software,^[56] the quadrupolar parameters are determined to $C_Q = 314$ kHz (quadrupolar coupling constant) and $\eta_Q = 0$ (asymmetry parameter). The ^{19}F -MAS NMR spectrum features a single resonance located at -100.9 ppm, accompanied by in toto four spinning sidebands of rather low intensity.

The ^{119}Sn -MAS NMR spectrum exhibits a manifold of signals from which the isotropic signal was identified via a variation of the spinning frequency as -1107 ppm. The chemical shift anisotropy (CSA) is determined as $d_{\text{CSA}} = 532$ ppm with a vanishing asymmetry parameter η_{CSA} .

The REDOR experiments were performed to establish the B–F bond for the tetrahedral BO_3F units. The constant time REDOR data plot is shown in Figure 4d. From a simulation using the SIMPSON simulation software a value for the ^{11}B – ^{19}F dipolar coupling $D = 10\,000$ Hz is obtained yielding a B–F distance of 1.54 Å confirming the X-ray diffraction data nicely. For a conventional REDOR experiment shown in Fig. S3 due to the extremely strong dipolar coupling the REDOR evolution curve reaches the plateau at rather short dipolar evolution times, leaving only a very limited number of data points for analysis, even at the high spinning frequencies adopted.

Thus the NMR data are found to be in perfect agreement with the crystal structure model. First of all, the appearance of a single signal for ^{119}Sn , ^{11}B , and ^{19}F confirms the presence of a single crystallographic site for each of these atoms. The B–F distance determined from the results of the REDOR experiment (1.54 Å) is within 10% of the distance as obtained from the X-ray data and clearly confirms the existence of a B–F bond. Together with the vanishing asymmetry parameter for the quadrupolar interaction of the ^{11}B nucleus this establishes a BO_3F tetrahedron with the threefold axis along the B–F bond. In addition, for ^{119}Sn , the vanishing asymmetry parameter η_{CSA} confirms the location of the tin atoms on a single site of (at least) threefold symmetry.

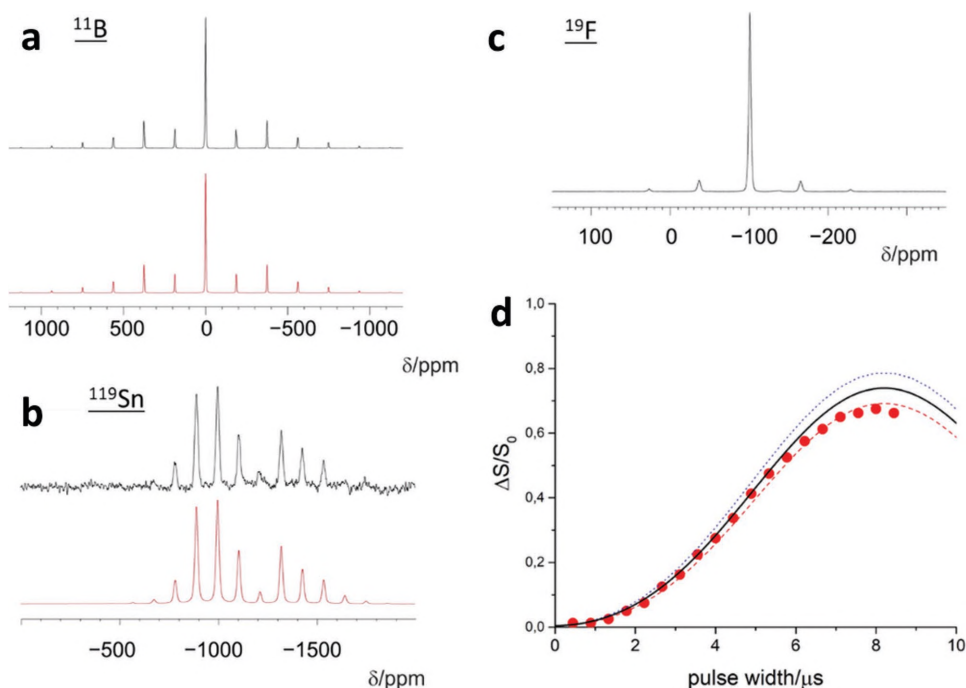


Figure 4. a–c) ^{11}B -, ^{119}Sn -, and ^{19}F -MAS NMR spectra of $\text{Sn}[\text{B}_2\text{O}_3\text{F}_2]$; the lower spectra are simulations using the DMFIT software, producing the following values: ^{11}B : $\delta_{\text{iso}} = 0$ ppm; $C_Q = 0.31$ MHz; $\eta_Q = 0.0$; ^{119}Sn : $\delta_{\text{iso}} = -1107$ ppm; $d_{\text{CSA}} = 532$ ppm; ^{19}F : $\delta_{\text{iso}} = -100.9$ ppm; d) $^{11}\text{B}\{^{19}\text{F}\}$ -REDOR data for $\text{Sn}[\text{B}_2\text{O}_3\text{F}_2]$: constant time REDOR using a variation of the ^{19}F pulse length; data (filled red circles) acquired at $\nu_{\text{MAS}} = 20$ kHz. The black line is a SIMPSON simulation^[55] assuming a ^{11}B - ^{19}F dipolar coupling of 10 000 Hz, translating into a B–F distance of 1.54 Å; the dotted line corresponds to a B–F distance of 1.51 Å, the dashed line to 1.56 Å.

2.4.2. Infrared Vibrational Spectroscopy

Infrared vibrational spectroscopy of $\text{Sn}[\text{B}_2\text{O}_3\text{F}_2]$ (Figure S4 top, Supporting Information) proves the absence of hydroxyl and trigonal-planar BO_3 groups, expected around 3700–3100 cm^{-1} and 1500–1350 cm^{-1} , respectively. The strong band at 960 cm^{-1} is assigned to the $\nu(\text{B}-\text{F})$ and $\nu_s(\text{B}-\text{O})$ vibrations. The 883 cm^{-1} band can be assigned to the $\nu_{\text{as}}(\text{B}-\text{O})$ and the 729 cm^{-1} band to $\delta(\text{O}-\text{B}-\text{O})$. $\delta(\text{O}-\text{B}-\text{F})$ is located at 517 cm^{-1} . While the observed IR bands are very broad, the respective Raman peaks (Figure S4 bottom, Supporting Information) comprise a far smaller full width at half maximum (FWHM). All observed and calculated bands and their assignment to the corresponding vibrations (derived from DFT calculations) are summarized in Table S6 (Supporting Information).

2.5. Thermal Analysis and Stability

The thermal stability of $\text{Sn}[\text{B}_2\text{O}_3\text{F}_2]$ was examined by thermogravimetric analysis and differential scanning calorimetry (Figure S5, Supporting Information). Under nitrogen $\text{Sn}[\text{B}_2\text{O}_3\text{F}_2]$ is stable up to 325 °C before decomposition starts. Heating to 450 °C results in a mass loss of $\approx 16.5\%$ which corresponds well with the suggested decomposition (Equation (1)) to BF_3 (the only volatile component at this temperature), B_2O_3 and $\text{Sn}_3[\text{B}_3\text{O}_7]\text{F}$, a tin borate fluoride we will present elsewhere.^[57] This conversion was also monitored by DSC. A further borate fluoride, namely $\text{Sn}_2[\text{B}_7\text{O}_{12}]\text{F}$, was discovered on

heating several times just above the onset of melting/decomposition of $\text{Sn}[\text{B}_2\text{O}_3\text{F}_2]$ in the DSC and represents apparently an intermediate product. This compound will also be presented elsewhere^[57]



$\text{Sn}[\text{B}_2\text{O}_3\text{F}_2]$ is stable in normal (not specifically dried) air, as repeated powder X-ray diffraction (XRD) measurements over twelve months revealed, while suspension of $\text{Sn}[\text{B}_2\text{O}_3\text{F}_2]$ in water results in decomposition to H_3BO_3 and several tin(II) and tin(IV) compounds, as SnF_2 hydrolyses in water.

3. Conclusion

We presented the very first tin fluorooxoborate $\text{Sn}[\text{B}_2\text{O}_3\text{F}_2]$ (TFB) based on a successful application of our approach toward non-centrosymmetric compounds using bidentate cations and layered polymeric anions with two termini with differing coordination strength. The astonishingly simple and highly acentric crystal structure of $\text{Sn}[\text{B}_2\text{O}_3\text{F}_2]$ also represents a new structure type adopting space group $P31m$ and was solved based on single-crystal X-ray diffraction data; the assignment of fluorine and oxygen was confirmed by electrostatic and theoretical calculations as well as spectroscopically by solid-state NMR. The absence of an inversion center was proven by SHG experiments yielding a nineteen-fold activity compared with quartz, thus providing the information that the SHG effect is even stronger

with respect to KDP. Moreover, the bandgap of $\text{Sn}[\text{B}_2\text{O}_3\text{F}_2]$ is well in the UV regime. The structure consisting of rather weakly coordinating fluorine atoms on one side might even enable the exfoliation of these layers further promoting NLO properties of such materials. Finally, the thermal and chemical stability of the new material is astonishingly high and the synthesis of phase-pure samples is surprisingly straightforward. Further experiments to obtain larger single-crystals as well as the characterization of the decomposition products are in train and will be published soon.

4. Experimental Section

Synthesis: $\text{Sn}[\text{B}_2\text{O}_3\text{F}_2]$ was obtained from SnF_2 (99%, Aldrich) and B_2O_3 (99.999%, Alfa Aesar) in a 1:1 molar ratio. Inside an argon glove box the starting materials were weighed out, ground in an agate mortar, pressed to a pellet, and filled into a silver crucible which was closed by a screw cap (inner volume ≈ 0.6 mL). Silver is used as crucible material due to its relatively high resistivity against fluorine containing compounds. The closed silver crucible was put into a fused silica-glass tube which was evacuated to $\approx 2 \times 10^{-2}$ mbar before closing the ampoule. Typically, 0.4 g educt-mixture was used and the ampoules were 7–10 cm long. For the synthesis of a microcrystalline powder (diameter of crystallites < 30 μm), the ampoule was heated in an electric tube furnace with 25 $^\circ\text{C h}^{-1}$ to 350 $^\circ\text{C}$ and maintained at this temperature for 72 h before cooling to room temperature with 25 $^\circ\text{C h}^{-1}$. The obtained product was a fine, crystalline, slightly beige powder.

Crystal Structure Determination: A colorless, block shaped crystal with dimensions $0.030 \times 0.020 \times 0.015$ mm^3 was selected under an optical microscope. Single-crystal X-ray diffraction data were collected on a Bruker D8 Venture diffractometer equipped with a SMART APEXII 4k CCD detector, using Mo K_α radiation; the data were corrected for absorption by applying a multiscan approach. The crystal structure of $\text{Sn}[\text{B}_2\text{O}_3\text{F}_2]$ was solved by direct methods, using the SHELXTL program package^[58] and refined with anisotropic displacement parameters for all atoms. The nonmerohedral twinning was solved by manually introducing the twin law $-1\ 0\ 0\ 0\ -1\ 0\ 0\ 0\ 1\ -4$ (BASF = 0.24082, 0.14988, 0.12135). Details of the X-ray data collection are summarized in Table S1 (Supporting Information). The positional and displacement parameters for all atoms are listed in the supplement (Tables S4 and S5, Supporting Information); further details of the crystal structure investigation of $\text{Sn}[\text{B}_2\text{O}_3\text{F}_2]$ may be obtained from the Fachinformationszentrum Karlsruhe, D-76344 Eggenstein-Leopoldshafen, Germany (e-mail: crysdata@fiz-karlsruhe.de) on quoting the depository number CSD-433766, the names of the authors, and citation of this publication.

Powder X-Ray Diffraction: The phase purity of the obtained samples was checked via powder X-ray diffraction (Figure S1, Supporting Information). Data were collected on a PANalytical Empyrean diffractometer using Cu K_α radiation (PIXcel^{3D2} $\times 2$ detector, steps of 0.026° , acquisition time 1.4 s per step, soller slits 0.02° , fixed divergence slit 0.0625° , Bragg-Brentano geometry). The generator was driven at 40 kV and 40 mA. The samples were finely ground and prepared on a zero background sample holder.

Spectroscopy: Solid State NMR Spectroscopy: ^{11}B -, ^{19}F -, and ^{119}Sn -MAS NMR spectra were recorded on a Varian VNMRs 500 NMR spectrometer operating at Larmor frequencies of 160.37 MHz (^{11}B), 187.55 MHz (^{119}Sn), and 470.3 MHz (^{19}F). All measurements were performed employing a Varian 1.6 mm T3 MAS NMR probe and spinning speeds of 20 and 30 kHz. The repetition times were set to 30, 125, and 500 s for ^{11}B , ^{19}F , and ^{119}Sn , respectively, with pulse lengths of 0.5, 2.25, and 2.0 μs . Spectra were referenced using CFCl_3 (^{19}F), $\text{BF}_3 \cdot \text{Et}_2\text{O}$ (^{11}B) and solid SnF_2 (^{119}Sn , -604 ppm) as references. The ^{11}B / ^{19}F -constant time REDOR experiments were performed with π -pulse lengths of 4.5 and 8 μs for ^{11}B and ^{19}F , employing spinning frequencies of 20 and 30 kHz. From the various different versions of constant time REDOR, the VPD

version (variable pulse delay) was employed. Like conventional REDOR, constant time REDOR allows for the determination of the heteronuclear ^{11}B - ^{19}F dipole coupling and hence the determination of the internuclear distance.^[59] The result from a rotor-synchronized spin-echo experiment for the observed (^{11}B) nuclei defines the full echo intensity S_0 which is then compared to a spectrum resulting from an experiment in which the heteronuclear dipolar coupling between the nuclei ^{11}B and ^{19}F has been reintroduced via rotor-synchronized pulses (^{19}F -channel) in addition to the ^{11}B spin-echo pulses. The difference of the spectra from the two experiments then only contains contributions from ^{11}B nuclei experiencing a dipolar coupling to ^{19}F nuclei. The magnitude of the REDOR effect depends on the strength of the dipolar coupling, the length of the applied ^{19}F pulses and the dipolar evolution time. In conventional REDOR, π -pulses are used and the dipolar evolution time is varied via the number of rotor cycles and the MAS frequency. The resulting REDOR evolution curves can then be analyzed to evaluate the magnitude of the dipolar coupling. In the case of extremely large dipolar coupling constants (as to be expected for direct B-F-bonding), however, the REDOR curve very quickly reaches the plateau, leaving only but a few data points for analysis. For cases like these constant time REDOR was developed.^[60,61] Here, the dipolar evolution time is kept fixed at some low value (2 or 4 rotor cycles), then varying the pulse length of the dephasing pulses. Via this deliberate decrease of the REDOR efficiency then the number of accessible data points can be dictated by the experimenter, thus allowing for a much more reliable data analysis. For details of the approach, the reader is referred to the literature.^[60,61]

Spectroscopy: IR Spectra: These were recorded on an Bruker EQUINOX 55 FT-IR-Spectrometer equipped with a Platinum ATR unit in the range 4000 – 400 cm^{-1} with a resolution of 4 cm^{-1} and 32 scans.

Spectroscopy: Raman Spectra: These were recorded on a Thermo Scientific DXR Raman-Microscope in the range 1800 – 60 cm^{-1} using a 532 nm laser operated with 10 mW power. The sample was illuminated for 3600 s (10-fold magnification, 50 μm pinhole aperture, high resolution grating (1800 lines mm^{-1}), spectral resolution 1 cm^{-1}). The background was corrected manually by subtracting a straight line.

The optical reflection spectrum for the bandgap measurement was measured using a Varian Cary 300 Scan UV/Vis spectrophotometer in the range of 200 – 800 nm and is shown in the supplement (Figure S6, Supporting Information).

Determination of NLO Properties: The powder SHG method developed by Kurtz and Perry^[53] is an established approach to estimate the nonlinear optical properties of new materials. The experimental setup for powder SHG measurements was described elsewhere.^[62] A Q-switched Nd:YLF laser system (Falcon 217D, Quantronix), operating at 1054 nm and a pulse width of 130 ns provides the fundamental wave. The generated SHG signal 527 nm was collected on three different sample areas to ensure that the powder was homogeneous. At each position several measurements were carried out, including measurements where the laser power was varied. The measured intensities were corrected by subtracting the background, which was measured between the pulses.

DFT Calculations: Quantum chemical calculations were performed in the framework of DFT using a linear combination of Gaussian-type functions (LCGTF) scheme as implemented in CRYSTAL14.^[63,64] The total energy calculations including full structural optimizations were performed with the GGA (PBE)^[65] and LDA (VWN) xc-functional^[66] and the Fock-exchange containing hybrid HSE06.^[67,68] Because of the layered nature of the compound and a better reproduction of experimental lattice constants, the van der Waals correction developed by Grimme was applied to PBE and HSE06 calculations.^[69] The convergence criterion considering the energy was set to 1×10^{-8} a.u. with a k-mesh sampling of $12 \times 12 \times 12$. All-electron basis sets as taken from (Sn-Basis),^[70–72] and the outermost coefficients of the contractions were optimized. Vibrational frequencies calculations with IR and Raman intensities were run on fully optimized structural models. Dispersion corrected (D2) PBE calculations yielded the best results, due to well-reproduced atomic distances and lattice parameters. The IR spectrum was simulated with the J-ICE application.^[73] The electronic structure was additionally assessed by the full potential local orbital (FPLO) method

as implemented in the FPLO-code (version 14.00-45)^[74] and atomic orbital contributions were projected onto the bands. Scalar-relativistic PBE calculations were carried out on a dense k-mesh of $12 \times 12 \times 12$. Further, a direct space analysis of the charge density was carried out by calculating the ELF with TOPOND^[75] interfaced to CRYSTAL14. 3D plots were visualized with XCrysDen.^[76] The ELF plot is shown in Figure S2 in the Supporting Information. First principles calculations were conducted based on the screened hybrid density functional of Heyd, Scuseria, and Ernzerhof (HSE06)^[68,77] using projector augmented wave (PAW)^[78] plane wave potentials as implemented in the Vienna ab initio Simulation Package (VASP).^[79–83] The calculations employed a 500 eV cut-off energy for the plane wave basis, a $6 \times 6 \times 6$ Γ -centered k-point mesh and 78 bands. The crystal structure was first optimized until the convergence criteria of 1×10^{-8} eV for the electronic structure and 1×10^{-2} eV \AA^{-1} for the ionic forces were achieved. The optical properties were then calculated based on the frequency dependent dielectric response including local field effects in the random-phase approximation (RPA).^[84] The resulting complex dielectric function $\mathcal{E}(\omega) = \mathcal{E}_1(\omega) + i\mathcal{E}_2(\omega)$ where \mathcal{E}_1 and \mathcal{E}_2 are the real and imaginary parts, respectively, can be transformed to obtain the absorbance, extinction coefficient, reflectivity, and refractive spectrum.^[85]

Thermal Analysis: The TG curve was recorded on a TA Instruments Q500 TGA in a 90 mL min^{-1} N_2 flow using an Al_2O_3 crucible. The DSC measurement was undertaken on a TA Instruments DSC 2920 in a 50 mL min^{-1} N_2 flow using a Netzsch standard Al pan with pierced lid.

Supporting Information

Supporting Information is available from the Wiley Online Library or from the author.

Acknowledgements

The authors thank Dr. Sabarinathan Venkatachalam for acquisition of the NMR data.

Conflict of Interest

The authors declare no conflict of interest.

Keywords

2D materials, nonlinear optics, silicate-analogous materials, structure–property relationships, tin fluorooxoborate

- [1] P. A. Franken, A. E. Hill, C. W. Peters, G. Weinreich, *Phys. Rev. Lett.* **1961**, 7, 118.
- [2] Y. Sun, Z. Yang, D. Hou, S. Pan, *RSC Adv.* **2017**, 7, 2804.
- [3] J. Hu, Z. Ma, R. Sa, Y. Zhang, K. Wu, *Dalton Trans.* **2017**, 46, 2635.
- [4] C. T. Chen, B. C. Wu, A. D. Jiang, G. M. You, *Sci. Sin. Ser. B* **1985**, 28, 235.
- [5] C. Chen, Y. Wu, A. Jiang, B. Wu, G. You, R. Li, S. Lin, *J. Opt. Soc. Am. B* **1989**, 6, 616.
- [6] J. J. D. Yoreo, A. K. Burnham, P. K. Whitman, *Int. Mater. Rev.* **2002**, 47, 113.
- [7] K. L. Seyler, J. R. Schaibley, P. Gong, P. Rivera, A. M. Jones, S. Wu, J. Yan, D. G. Mandrus, W. Yao, X. Xu, *Nat. Nanotechnol.* **2015**, 10, 407.
- [8] L. M. Malard, T. V. Alencar, A. P. M. Barboza, K. F. Mak, A. M. de Paula, *Phys. Rev. B* **2013**, 87, 201401.
- [9] Y. Li, Y. Rao, K. F. Mak, Y. You, S. Wang, C. R. Dean, T. F. Heinz, *Nano Lett.* **2013**, 13, 3329.
- [10] L. Mei, Y. Wang, C. Chen, B. Wu, *J. Appl. Phys.* **1993**, 74, 7014.
- [11] H. Yu, H. Wu, S. Pan, Z. Yang, X. Hou, X. Su, Q. Jing, K. R. Poeppelmeier, J. M. Rondinelli, *J. Am. Chem. Soc.* **2014**, 136, 1264.
- [12] C. Chen, Y. Wang, B. Wu, K. Wu, W. Zeng, L. Yu, *Nature* **1995**, 373, 322.
- [13] L. Li, G. Li, Y. Wang, F. Liao, J. Lin, *Chem. Mater.* **2005**, 17, 4174.
- [14] G. Cakmak, *Ph.D. thesis*, Max-Planck-Institut für Festkörperforschung, Stuttgart **2009**.
- [15] G. Cakmak, J. Nuss, M. Jansen, *Z. Anorg. Allg. Chem.* **2009**, 635, 631.
- [16] T. Pilz, M. Jansen, *Z. Anorg. Allg. Chem.* **2011**, 637, 2148.
- [17] T. Pilz, H. Nuss, M. Jansen, *J. Solid State Chem.* **2012**, 186, 104.
- [18] T. Pilz, M. Jansen, *Z. Anorg. Allg. Chem.* **2012**, 638, 1624.
- [19] G. Cakmak, T. Pilz, M. Jansen, *Z. Anorg. Allg. Chem.* **2012**, 638, 1411.
- [20] B. Andriyevsky, K. Doll, G. Cakmak, M. Jansen, A. Niemer, K. Betzler, *Phys. Rev. B* **2011**, 84, 125112.
- [21] B. Andriyevsky, T. Pilz, J. Yeon, P. S. Halasyamani, K. Doll, M. Jansen, *J. Phys. Chem. Solids* **2013**, 74, 616.
- [22] W. Xuefei, W. Ying, Z. Bingbing, Z. Fangfang, Y. Zhuhua, P. Shilie, *Angew. Chem., Int. Ed.* **2017**, 56, 14119.
- [23] G. Shi, F. Zhang, B. Zhang, D. Hou, X. Chen, Z. Yang, S. Pan, *Inorg. Chem.* **2017**, 56, 344.
- [24] B. Zhang, G. Shi, Z. Yang, F. Zhang, S. Pan, *Angew. Chem., Int. Ed.* **2017**, 56, 3916.
- [25] T. Pilz, *Ph.D. thesis*, MPI Stuttgart **2013**.
- [26] S. G. Jantz, L. van Wüllen, A. Fischer, E. Libowitzky, E. J. Baran, M. Weil, H. A. Höpfe, *Eur. J. Inorg. Chem.* **2016**, 2016, 1121.
- [27] F. Liang, L. Kang, P. Gong, Z. Lin, Y. Wu, *Chem. Mater.* **2017**, 29, 7098.
- [28] S. G. Jantz, F. Pielhofer, L. van Wüllen, R. Wehrich, M. J. Schäfer, H. A. Höpfe, *Chem. Eur. J.* **2018**, 24, 443.
- [29] H. Wu, H. Yu, Q. Bian, Z. Yang, S. Han, S. Pan, *Inorg. Chem.* **2014**, 53, 12686.
- [30] R. Cong, Y. Wang, L. Kang, Z. Zhou, Z. Lin, T. Yang, *Inorg. Chem. Front.* **2015**, 2, 170.
- [31] G. Shi, Y. Wang, F. Zhang, B. Zhang, Z. Yang, X. Hou, S. Pan, K. R. Poeppelmeier, *J. Am. Chem. Soc.* **2017**, 139, 10645.
- [32] Z. Zhizhong, W. Ying, Z. Bingbing, Y. Zhuhua, P. Shilie, *Angew. Chem., Int. Ed.* **2018**, 57, 6577.
- [33] W. Ying, Z. Bingbing, Y. Zhuhua, P. Shilie, *Angew. Chem., Int. Ed.* **2018**, 57, 2150.
- [34] M. Miriding, Z. Min, Z. Bingbing, W. Liying, Y. Zhuhua, Z. Xin, P. Shilie, *Angew. Chem., Int. Ed.* **2018**, 57, 6095.
- [35] M. Luo, F. Liang, Y. Song, D. Zhao, F. Xu, N. Ye, Z. Lin, *J. Am. Chem. Soc.* **2018**, 140, 3884.
- [36] H. A. Höpfe, *Solid State Sci.* **2005**, 7, 1209.
- [37] H. A. Höpfe, *Z. Anorg. Allg. Chem.* **2005**, 631, 1272.
- [38] H. A. Höpfe, S. J. Sedlmaier, *Inorg. Chem.* **2007**, 46, 3467.
- [39] H. A. Höpfe, *J. Solid State Chem.* **2009**, 182, 1786.
- [40] J. S. Knyrim, P. Becker, D. Johrendt, H. Huppertz, *Angew. Chem., Int. Ed.* **2006**, 45, 8239.
- [41] M. Mellini, G. Cressey, F. J. Wicks, B. A. Cressey, *Mineral. Mag.* **2016**, 74, 277.
- [42] M. Schroeder, H. Hillebrecht, *J. Am. Chem. Soc.* **2009**, 131, 12172.
- [43] P. Schultz, V. Sagawe, H. Hillebrecht, *Solid State Sci.* **2013**, 26, 121.
- [44] R. D. Shannon, *Acta Crystallogr.* **1976**, B32, 751.

- [45] T. Balić-Žunić, E. Makovicky, *Acta Crystallogr. B* **1996**, *52*, 78.
- [46] E. Makovicky, T. Balić-Žunić, *Acta Crystallogr. B* **1998**, *54*, 766.
- [47] R. D. Shannon, C. T. Prewitt, *Acta Crystallogr. B* **1969**, *25*, 925.
- [48] R. Hoppe, *Angew. Chem., Int. Ed.* **1966**, *5*, 95.
- [49] R. Hoppe, *Angew. Chem., Int. Ed.* **1970**, *9*, 25.
- [50] R. Hübenthal, *MAPLE, Program for the Calculation of the Madelung Part of Lattice Energy* **1993**.
- [51] R. C. McDonald, H. H. K. Hau, K. Eriks, *Inorg. Chem.* **1976**, *15*, 762.
- [52] S. L. Strong, R. Kaplow, *Acta Crystallogr. B* **1968**, *24*, 1032.
- [53] S. K. Kurtz, T. T. Perry, *J. Appl. Phys.* **1968**, *39*, 3798.
- [54] L. Bayarjargal, B. Winkler, *Z. Kristallogr. - Cryst. Mater.* **2014**, *229*, 92.
- [55] M. Bak, J. T. Rasmussen, N. C. Nielsen, *J. Magn. Reson.* **2000**, *147*, 296.
- [56] D. Massiot, F. Fayon, M. Capron, I. King, S. Le Calvé, B. Alonso, J.-O. Durand, B. Bujoli, Z. Gan, G. Hoatson, *Magn. Reson. Chem.* **2002**, *40*, 70.
- [57] S. G. Jantz, H. A. Höpfe, et al., *Chem. Eur. J.* **2018**, submitted.
- [58] G. Sheldrick, *Acta Crystallogr. A* **2008**, *64*, 112.
- [59] T. Gullion, J. Schaefer, *J. Magn. Reson.* **1989**, *81*, 196.
- [60] T. Echelmeyer, S. Wegner, L. van Wüllen, *Annual Reports on NMR Spectroscopy*, Vol. 75 (Ed: G. A. Webb), Academic Press, Oxford **2012**, pp. 1–23.
- [61] T. Echelmeyer, L. van Wüllen, S. Wegner, *Solid State Nucl. Magn. Reson.* **2008**, *34*, 14, special issue honoring Professor Hans-Heinrich Limbach on the occasion of his 65th birthday.
- [62] L. Bayarjargal, B. Winkler, E. Haussühl, R. Boehler, *Appl. Phys. Lett.* **2009**, *95*, 061907.
- [63] R. Dovesi, V. R. Saunders, C. Roetti, R. Orlando, C. M. Zicovich-Wilson, F. Pascale, B. Civalleri, K. Doll, N. M. Harrison, I. J. Bush, P. D'Arco, M. Llunell, M. Causà, Y. Noël, *CRYSTAL14 User's Manual*, University of Torino, Torino, Italy **2014**.
- [64] R. Dovesi, R. Orlando, A. Erba, C. M. Zicovich-Wilson, B. Civalleri, S. Casassa, L. Maschio, M. Ferrabone, M. D. L. Pierre, P. D'Arco, Y. Noël, M. Causà, M. Rérat, B. Kirtman, *Int. J. Quantum Chem.* **2014**, *114*, 1287.
- [65] J. P. Perdew, K. Burke, M. Ernzerhof, *Phys. Rev. Lett.* **1996**, *77*, 3865.
- [66] S. H. Vosko, L. Wilk, M. Nusair, *Can. J. Phys.* **1980**, *58*, 1200.
- [67] A. D. Becke, *Phys. Rev. A* **1988**, *38*, 3098.
- [68] J. Heyd, G. E. Scuseria, M. Ernzerhof, *J. Chem. Phys.* **2003**, *118*, 8207.
- [69] S. Grimme, *J. Comput. Chem.* **2006**, *27*, 1787.
- [70] R. Orlando, R. Dovesi, C. Roetti, V. R. Saunders, *J. Phys.: Condens. Matter* **1990**, *2*, 7769.
- [71] J. Scaranto, S. Giorgianni, *J. Mol. Struct.: THEOCHEM* **2008**, *858*, 72.
- [72] R. Nada, C. R. A. Catlow, C. Pisani, R. Orlando, *Modell. Simul. Mater. Sci. Eng.* **1993**, *1*, 165.
- [73] P. Canepa, R. M. Hanson, P. Ugliengo, M. Alfredsson, *J. Appl. Crystallogr.* **2014**, *44*, 225.
- [74] K. Koepernik, H. Eschrig, *Phys. Rev. B* **1999**, *59*, 1743.
- [75] C. Gatti, S. Cassassa, Topond14, <http://www.crystal.unito.it/topond/topond.pdf> (accessed: October 2016).
- [76] A. Kokalj, *Comput. Mater. Sci.* **2003**, *28*, 155.
- [77] A. V. Krukau, O. A. Vydrov, A. F. Izmaylov, G. E. Scuseria, *J. Chem. Phys.* **2006**, *125*, 224106.
- [78] P. E. Blöchl, *Phys. Rev. B* **1994**, *50*, 17953.
- [79] G. Kresse, D. Joubert, *Phys. Rev. B* **1999**, *59*, 1758.
- [80] G. Kresse, J. Furthmüller, *Phys. Rev. B* **1996**, *54*, 11169.
- [81] G. Kresse, J. Furthmüller, *Int. J. Comput. Mater. Sci. Surf. Eng.* **1996**, *6*, 15.
- [82] G. Kresse, J. Hafner, *Phys. Rev. B* **1993**, *47*, 558.
- [83] G. Kresse, J. Hafner, *Phys. Rev. B* **1994**, *49*, 14251.
- [84] J. Harl, G. Kresse, *Phys. Rev. Lett.* **2009**, *103*, 056401.
- [85] F. Wooten, *Optical Properties of Solids*, Academic Press, New York **1972**.